NUCL SCI TECH (2021) 32:66
https://doi.org/10.1007/s41365-021-00897-9

α-clustering effect on flows of direct photons in heavy-ion collisions

Chen-Zhong Shi[1,2,3] · **Yu-Gang Ma**[1,2]

Received: 10 March 2021 / Revised: 16 April 2021 / Accepted: 22 April 2021 / Published online: 23 June 2021

Abstract In this study, we reconstruct the γ-photon energy spectrum, which is in good agreement with the experimental data of ^{86}Kr + ^{12}C at E/A = 44 MeV within the framework of the modified EQMD model. The directed and elliptic flows of free protons and direct photons were investigated by considering the α-clustering structure of ^{12}C. Compared with free protons, direct photon flows provide clearer information about the early stage of a nuclear reaction. The difference in the collective flows between different configurations of ^{12}C is observed in this study. This indicates that the collective flows of direct photons are sensitive to the initial configuration. Therefore, the γ bremsstrahlung process might be taken as an alternative probe to investigate the α-clustering structure in a light nucleus from heavy-ion collisions within the Fermi-energy region.

This work was supported by the Guangdong Major Project of Basic and Applied Basic Research (No. 2020B0301030008), the National Natural Science Foundation of China (Nos. 11890710, 11890714, and 11961141003), and the Strategic Priority Research Program of the CAS (No. XDB34000000).

✉ Yu-Gang Ma
mayugang@fudan.edu.cn

[1] Shanghai Institute of Applied Physics, Chinese Academy of Sciences, Shanghai 201800, China

[2] Key Laboratory of Nuclear Physics and Ion-beam Application (MOE), Institute of Modern Physics, Fudan University, Shanghai 200433, China

[3] University of the Chinese Academy of Sciences, Beijing 100080, China

Keywords Nuclear reaction · Direct photon · Collective flow · α-clustering configuration

1 Introduction

The α-clustering configuration in a light nucleus has attracted considerable attention for an extremely long time. During the 1930s, even before the discovery of neutrons, this concept was first assumed by Gamow [1] and discussed by Bethe and Bacher [2, 3] because of the high stability of the α-cluster around neighboring light nuclei. Following this idea, an image of the nuclear molecular state [4] based on the α-α interaction, which presents as a repulsive force within short and long ranges or as an attractive force within the intermediate range, has been established. Such a simple description is in good agreement with the binding energies of the saturated nuclei composed of multiple-α clusters. However, these α-clustering structures were not observed in the ground states of the nucleus but were observed in excited states close to the α-decay thresholds. Among the numerous α-clustering nuclei, ^{12}C is one of the most popular, which is related to its important role in the process of nucleosynthesis in astrophysics [5–8], that is, the triple-α process.

Currently, there are many models or theories capable of producing α-clustering nuclei, such as antisymmetrized molecular dynamics (AMD) [9], fermionic molecular dynamics (FMD) [10], and extended quantum molecular dynamics (EQMD) [11]. Specifically, for ^{12}C, the chain structure is usually considered an excited state, and thus we only consider the triangle and sphere configurations in this study. Many studies aiming at the α-cluster have recently been conducted using a framework of the transport models.

In these studies, giant dipole resonance [12, 13], photon disintegration [14], HBT correlation [15–17], and collective flows [18–24] have been suggested as useful probes for investigating the α-clustering configuration in a light nucleus.

On the other hand, for an anisotropic flow itself, also known as a collective flow, it has been widely investigated in nuclear physics from more than 10 *A*MeV to several *A* TeV [25, 26]. Its earliest ideas [27] can be traced back to the 1950s, when fluid dynamical models were used to describe the collisions between nucleons and nuclei. During the 1970s, this concept was extended to heavy-ion reactions [28], but was not convincingly observed in the laboratory until the 1990s [29, 30]. It is now well known that an anisotropic flow can be considered an important observable in nuclear physics, e.g., studies on an in-medium cross section [31], viscosity coefficient [32], equation of state (EOS) [33], and reaction mechanism [34] within the low- and medium-energy regions. Moreover, such a collective movement is also significant for studying the QGP within the relativistic energy range because of its sensitivity to early partonic dynamics [35–37]. Therefore, the idea of using an anisotropic flow to investigate the different initial geometries of a light nucleus [18–20] has been proposed for relativistic energies.

In such studies, all observed particles are hadrons that are influenced by the surrounding nuclear matter in the final stage, particularly within the Fermi energy region. However, direct photons produced during the early stages of heavy-ion reactions are seldom influenced by the surrounding nuclear matter. In our previous studies [38–41], an anti-correlation between direct photons and free protons was observed in symmetric collision systems. This indicates that direct photons are highly related to the collective flow of nucleons and can be used as an alternative probe to find a trace of α-cluster structures in light nuclei.

In the present research, the geometric effects of two different configurations on the collective flow of direct photons for the reaction of ^{86}Kr + ^{12}C at E/A = 44 MeV [42] were studied. The remainder of this article is arranged as follows: the model and method are briefly introduced in Sect. 2, the results and discussion are given in Sect. 3, and a summary is provided in Sect. 4.

2 The model and method description

2.1 EQMD model

The EQMD model [11] is a type of QMD-type approach whose equations of motion are determined by the time-dependent variational principle (TDVP) [10]. In the EQMD model, the nucleon is represented by a coherent state, and the total system is a direct product of each nucleon, which is similar to most QMD-type models. A phenomenological Pauli potential has been added to satisfy the ground state fermion properties. In addition, dynamic wave packets are implied in this model by replacing fixed wave packets in traditional QMD modes. The nucleon wave function and total wave function can be expressed as follows:

$$\begin{aligned}\varphi_i(\mathbf{r}_i) &= \left(\frac{v_i + v_i^*}{2\pi}\right)^{3/4} \exp\left[-\frac{v_i}{2}(\mathbf{r}_i - \mathbf{R}_i)^2 + \frac{i}{\hbar}\mathbf{P}_i \cdot \mathbf{r}_i\right], \\ \Psi &= \prod_i \varphi_i(\mathbf{r}_i).\end{aligned} \tag{1}$$

Here, $\mathbf{R}_i$ and $\mathbf{P}_i$ are the mean values of the wave packet belonging to the ith nucleon in the phase space. Correspondingly, $v_i = \frac{1}{\lambda_i} + i\delta_i$ is the complex wave packet width. Under the time-dependent variation principle, the propagation of each nucleon can be described as follows:

$$\begin{aligned}\dot{\mathbf{R}}_i &= \frac{\partial H}{\partial \mathbf{P}_i} + \mu_{\mathrm{R}}\frac{\partial H}{\partial \mathbf{R}_i}, \dot{\mathbf{P}}_i = -\frac{\partial H}{\partial \mathbf{R}_i} + \mu_{\mathrm{P}}\frac{\partial H}{\partial \mathbf{P}_i}, \\ \frac{3\hbar}{4}\dot{\lambda}_i &= -\frac{\partial H}{\partial \delta_i} + \mu_\lambda \frac{\partial H}{\partial \lambda_i}, \frac{3\hbar}{4}\dot{\delta}_i = \frac{\partial H}{\partial \lambda_i} + \mu_\delta \frac{\partial H}{\partial \delta_i}.\end{aligned} \tag{2}$$

Here, H is the expected value of the Hamiltonian, and $\mu_{\mathbf{R}}$, $\mu_{\mathbf{P}}$, μ_λ, and μ_δ are the friction coefficients. In the friction cooling process, these coefficients are negative for obtaining a stable nucleus, whereas in the subsequent nuclear reaction simulation stage, these coefficients are zero to maintain the energy conservation of the system. The expected value of the Hamiltonian of the EQMD model can be expressed as follows:

$$\begin{aligned}H &= \left\langle \Psi \middle| \sum_i -\frac{\hbar^2}{2m}\nabla_i^2 - \hat{T}_{\mathrm{zero}} + \hat{H}_{\mathrm{int}} \middle| \Psi \right\rangle \\ &= \sum_i \frac{\mathbf{P}_i^2}{2m} + \frac{3\hbar^2\left(1 + \lambda_i^2\delta_i^2\right)}{4m\lambda_i} - T_{\mathrm{zero}} + H_{\mathrm{int}},\end{aligned} \tag{3}$$

where the first three terms represent the expected values of the kinetic energy of each nucleon. The first term is the center momentum of the wave packet $\langle\hat{\mathbf{p}}_i\rangle^2/2m$, the second term is the contribution of the dynamic wave packet $\left(\langle\hat{\mathbf{p}}_i^2\rangle - \langle\hat{\mathbf{p}}_i\rangle^2\right)/2m$, and the third term $-T_{\mathrm{zero}}$ is the zero-point center-of-mass kinetic energy, which can be expressed as

$$T_{\text{zero}} = \sum_i \frac{t_i}{M_i},$$
$$t_i = \frac{\left\langle \phi_i \middle| \hat{\mathbf{p}}^2 \middle| \phi_i \right\rangle}{2m} - \frac{\langle \phi_i | \hat{\mathbf{p}} | \phi_i \rangle^2}{2m}. \tag{4}$$

Here, M_i is the "mass number" and its detailed definition is as follows [11]:

$$M_i = \sum_j F_{ij},$$
$$F_{ij} = \begin{cases} 1 & \left(|\mathbf{R}_i - \mathbf{R}_j| < a\right) \\ e^{-\left(|\mathbf{R}_i - \mathbf{R}_j| - a\right)^2 / b} & \left(|\mathbf{R}_i - \mathbf{R}_j| \geqslant a\right) \end{cases}, \tag{5}$$

where the parameters $a = 1.7$ fm and $b = 4$ fm^2 (Fig. 1).

In addition, we also show the "mass number" as a function of the distance between two nucleons. It is obvious that the "mass number" increases as the two nucleons approach; otherwise, it decreases. Comparing the second term with the third, it is not difficult to see that they are only different with a factor of $\frac{1}{M_i}$ and a minus sign. When i and j are the same particles, their value is 1. Therefore, if a nucleus breaks away from the collision and becomes a free particle, the "mass number" decreases to 1. Then, the zero-point kinetic energy offsets the second item contribution. This is also related to the momentum re-extraction later.

The last term represents the mean field potential adopted in the EQMD model. In this model, only an extremely simple potential form was used, for example, two-body and density-dependent terms from the Skyrme, Coulomb, symmetry, and Pauli potential. A detailed description is provided in Ref. [11]. We used the second set of parameters in this study. It should be emphasized that dynamical wave packets also contribute to the kinetic energy. This treatment is extremely different from most QMD-type models. For this reason, the energy spectrum of direct photons is unreasonable, as reported in our previous study [43]. Therefore, it is necessary to consider this effect self-consistently during the in-elastic process. As to why the zero-point kinetic energy was introduced in original EQMD model, please refer to [44].

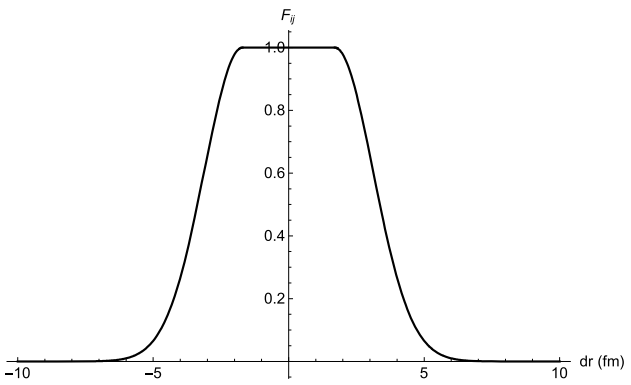

Fig. 1 The "mass" number as a function of the distance between two nucleons. Here $dr = R_i - R_j$

2.2 Bremsstrahlung process in the EQMD

To make the bremsstrahlung contributions for direct photons, only the first instant proton-neutron collision was considered in this study. The elementary double differential cross-section adopted was improved by Bauer et al. [45] as follows:

$$\frac{\mathrm{d}^2\sigma^{\text{elem}}}{\mathrm{d}E_\gamma \mathrm{d}\Omega_\gamma} = \alpha_{\text{c}} \frac{R^2}{12\pi} \frac{1}{E_\gamma} \left(2\beta_{\text{f}}^2 + 3\sin^2\theta_\gamma \beta_{\text{i}}^2\right). \tag{6}$$

Here, R represents the radius of the hard sphere, α_{c} represents the fine structure constant, and β_{i} and β_{f} represent the velocity of protons at the initial and final stages in the rest of the proton-neutron frame. In addition, θ_γ represents the angle between the outgoing photon and the direction of the incident proton in the same rest frame. Then, combining with the Pauli-blocking in the final state of scattered protons and neutrons, the probability of a photon emitted from a p-n collision can be deduced as follows:

$$\int \frac{\mathrm{d}\Omega_e}{4\pi} \frac{1}{\sigma_{NN}} \frac{\mathrm{d}^2\sigma^{\text{elem}}}{\mathrm{d}E_\gamma \mathrm{d}\Omega_\gamma} \times [1 - S_3(\mathbf{r}_3, \mathbf{k}_3, t)][1 - S_4(\mathbf{r}_4, \mathbf{k}_4, t)]. \tag{7}$$

Here, σ_{NN} is the elemental nucleon-nucleon cross section; $\mathbf{r}_3$, $\mathbf{r}_4$, $\mathbf{k}_3$, and $\mathbf{k}_4$ are the scattered nucleons phase-space coordinates in the final state; and S_3 and S_4 are the effective occupation fractions. The parameters adopted are the same as those used by Bauer et al. [45]. From our previous study [43], the general approach for treating two-body inelastic scattering is inapplicable to the EQMD model because of the effects of the dynamic wave packets. Therefore, a feasible method and proof of its effectiveness have been proposed. To avoid considering the geometric condition of two-body scattering after sampling, a slight adjustment was made in this study. We assume that the two particles are in the same position after sampling if they are judged to have undergone a collision. In other words, position sampling of scattering nucleons was applied before their momentum sampling. Then, the coupling term of the coordinate and momentum, which has previously been neglected, was introduced. The Wigner function of the EQMD can be written as follows [43]:

$$w(\mathbf{r},\mathbf{p}) = \left(\frac{1}{\pi\hbar}\right)^3 \sum_i^A \exp\Big[-\frac{1+\lambda_i^2\delta_i^2}{\lambda_i}(\mathbf{r}-\mathbf{R}_i)^2 - \frac{2\lambda_i\delta_i}{\hbar}(\mathbf{r}-\mathbf{R}_i)(\mathbf{p}-\mathbf{P}_i) - \frac{\lambda_i}{\hbar^2}(\mathbf{p}-\mathbf{P}_i)^2\Big]. \tag{8}$$

Here, w represents the phase-space density, which is the closest analogue to the classical phase-space density. The position of the scattered nucleons can be determined by the density overlap of the two nucleons as follows:

$$w_{ij}(\mathbf{r}) = \frac{\rho_i(\mathbf{r})\rho_j(\mathbf{r})}{\int \rho_i(\mathbf{r})\rho_j(\mathbf{r})d\mathbf{r}} = \left(\frac{\lambda_i+\lambda_j}{\pi\lambda_i\lambda_j}\right)^{3/2} \exp\left\{-\frac{\lambda_i+\lambda_j}{\lambda_i\lambda_j}\left(\mathbf{r}-\frac{\lambda_\mathbf{i}\mathbf{R_j}+\lambda_\mathbf{j}\mathbf{R_i}}{\lambda_\mathbf{i}+\lambda_\mathbf{j}}\right)^\mathbf{2}\right\}. \tag{9}$$

Here, $\rho_i(\mathbf{r})\rho_j(\mathbf{r})$ is the density overlap, and the integration of the denominator ensures a probability normalization. It is then easy to deduce that the momentum distribution of the ith nucleon belongs to the conditional probability rule, i.e.,

$$w_i(\mathbf{p}) = \frac{w_i(\mathbf{r},\mathbf{p})}{w_i(\mathbf{r})} = \left(\frac{\lambda_i}{\pi\hbar^2}\right)^{3/2} \exp\left\{-\frac{\lambda_i}{\hbar^2}[p-(\mathbf{P}_i-\delta_i\hbar\mathbf{r}+\delta_i\hbar\mathbf{R}_i)]\right\}, \tag{10}$$

where $w_i(\mathbf{r},\mathbf{p})$ represents the Wigner density of the ith nucleon at point $(\mathbf{r},\mathbf{p})$ in the phase space. Compared with the previous study, this requires one more sampling in the coordinate space. In addition, $w_i(\mathbf{p})$ represents the momentum distribution of the ith nucleon with the coordinate position at $\mathbf{r}$. Now, we obtain the momentum of the ith nucleon randomly as follows:

$$\begin{aligned}\mathbf{r}_i &= \mathbf{r}\\ \Delta\mathbf{p} &= \mathbf{p}-\mathbf{P}_i\\ \mathbf{p}_i &= \mathbf{P}_i + \Delta\mathbf{p}\times\sqrt{1-\frac{1}{M_i}}.\end{aligned} \tag{11}$$

The square root term considers the zero-point center-of-mass kinetic energy in Eq. 4. This treatment can be applied to both free nucleons and nucleons in a medium. In addition, when a nucleon becomes free, it automatically degenerates into a traditional form, that is, the center momentum of the wave packet is used as the momentum of the nucleon because its zero-point kinetic energy covers its dynamic wave packet contribution to the kinetic energy, as described in Sect. 2.1. This property is automatically satisfied when we consider the zero-point kinetic energy, which is related to the design of the Hamiltonian by Maruyama et al. [11]. When a nucleon becomes a free nucleon, its central coordinates can be directly used to calculate its collective motion, which is consistent with the study by Guo et al. [22, 23].

Strictly speaking, the coordinates and momentum of a nucleon should be sampled adequately according to its own Wigner function (Eq. 8), as in most BUU-type models. Meanwhile, it should also consider the zero-point kinetic energy. The deduction is shown in Appendix 1. However, to simplify the calculation, we only sample the following Eqs. 9, 10 and 11, the coordinate space sampling of which is limited. As another advantage of Eq. 9, the in-medium effect can be easily included by assuming that the two nucleons collide at the same point.

In addition, Pauli-blocking needs to be reconsidered because of the information loss of the wave packet after sampling. In this study, we calculated the effective occupation fraction as follows:

$$S_i = h^3 \times \sum_{j\neq i} \delta_{\tau_i,\tau_j}\delta_{s_i,s_j} w_j(\mathbf{R}_i',\mathbf{P}_i'). \tag{12}$$

Here, $\mathbf{R}_i'$ and $\mathbf{P}_i'$ are the coordinates and momentum of the scattered nucleons in the final state, respectively. In addition, w_j is the density of the Wigner function contributed by the other nucleons to the phase-space point $(\mathbf{R}_i',\mathbf{P}_i')$, where h^3 is the volume size. A more detailed description can be found in our previous study [43]. However, it should be noted that this method is an extremely simple way to include the fermionic properties of nucleons.

2.3 Anisotropic flow of direct photons

Anisotropic flow can be characterized by the Fourier expansion of the emitted particles as follows [46]:

$$E\frac{\mathrm{d}^3N}{\mathrm{d}^3p} = \frac{1}{2\pi}\frac{\mathrm{d}^2N}{p_\mathrm{T}\mathrm{d}p_\mathrm{T}\mathrm{d}y}\left(1+\sum_{i=1}^{N} 2v_n\cos[n(\phi-\Psi_n)]\right), \tag{13}$$

where ϕ is the azimuthal angle between the emitted particle and the reaction plane, and v_n represents different orders of the Fourier coefficients, which can be deduced if assuming that the reaction plane is the $x-z$ plane, that is, $\Psi_n = 0$ in our calculation, as follows:

$$\begin{aligned}v_1 &= \langle\cos([\phi-\Psi_1])\rangle = \left\langle\frac{p_x}{p_\mathrm{T}}\right\rangle,\\ v_2 &= \langle\cos(2[\phi-\Psi_2])\rangle = \left\langle\frac{p_x^2-p_y^2}{p_\mathrm{T}^2}\right\rangle.\end{aligned} \tag{14}$$

Here, we only show the first- and second-order coefficients of the Fourier expansion, $\langle\ldots\rangle$ represents a statistical

averaging over all emitted particles in all events, and $p_T = \sqrt{p_x^2 + p_y^2}$ is the transverse momentum of the emitted particles. By convention, it defines the directed flow of the particles emitted forward as a positive value when the repulsion dominates for free protons or neutrons [25]. A negative value is presented when attraction dominates for the symmetry system. We also follow this rule in this study, although an asymmetry system is used. The actual case for hadrons is more complicated for asymmetric systems.

In Ref. [18], the authors use carbon to collide lead within the relativistic energy region. The shape of the created fireball in the transverse plane then reflects the shape of ^{12}C. The hot zone formed expands outward along the density-gradient direction. Therefore, the harmonic flow analysis can indirectly reflect the spatial deformation of the initial state [18]. However, in a low-energy region where the attraction dominates, the formation mechanism of the collective flow is extremely different [47, 48]. This is the result of the competition between the mean-field potential and the two-body collision. The created compressed zone rotates along the *y*-direction perpendicular to the reaction plane owing to the angular momentum effect of a finite impact parameter. Finally, the particles prefer a side splashing in the reaction plane.

3 Results and discussion

Figure 2 shows the density contour of different configurations of ^{12}C, where the panel (a) corresponds to a triangular configuration and panel (b) response to a spherical configuration. Obviously, there are three cores far from the central region in the triangular configuration of 3α clusters. By contrast, there is only one core in the central region in the spherical configuration case. These two configurations

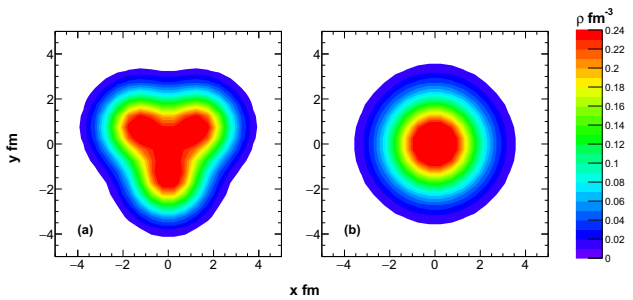

Fig. 2 (Color online) Density distribution of ^{12}C with configurations of (a) α-clustered triangle and (b) sphere. The configuration of α-clustered ^{12}C is rotated to a plane perpendicular to its symmetry axis in the coordinate space

also appear in the AMD simulation [49]. With the increase in the excitation energy, the transition from a spherical configuration into the triangular configuration was observed. However, it is worth noting that the ground state of ^{12}C initialized by the friction cooling process in the EQMD model is triangle configuration of 3α. Strictly speaking, the EQMD model does not provide complete Fermi properties owing to the phenomenological Pauli-potential used instead of the anti-symmetry of the wave function. However, in comparison with the AMD and FMD, it has more significant computing advantages.

The different types of configurations given by the EQMD model are random. Before the friction cooling process, the positions of the nucleons are sampled within a solid sphere, and their momentum is sampled according to the Thomas-Fermi gas model. The cooling path is influenced by the initial coordinates and momentum. Therefore, all configurations can be created during the batch initialization processes, but only the specific configurations are chosen as the initial input nuclei.

Table 1 lists the binding energy and the root mean square (r.m.s) radius of ^{12}C from the experimental measurement as well as the results calculated by the EQMD for different configurations. The r.m.s. radii of different configurations are near. Although the binding energy of the sphere configuration adopted in this work is approximately 0.8 MeV higher than that of a triangular configuration, they are both close to the experimental value. It should be emphasized that the energy level of different configurations is not studied in detail in this paper , but focus is given to the geometric effects during a heavy-ion collision.

Figure 3a–c shows the density, momentum, and width of the wave packet distribution of different configurations for ^{12}C. For comparison, the Woods-Saxon situation has also been drawn as a solid black line in panels (a) and (b). In panel (a), the differences in the density distribution among the three configurations are clearly observed. In the case of the Woods-Saxon distribution, the density remains almost constant at $0.16/\text{fm}^3$ near the central region. However, in the case of a triangular configuration, the density is higher. In addition, in the case of a spherical configuration, the

Table 1 The values of binding energy and r.m.s radii of different configurations initialized by the EQMD as well as the experimental measurement

	E/A (MeV)	*R.M.S* (fm)
Triangle	− 7.721	2.313
Sphere	− 6.982	2.333
Exp.	− 7.68	2.46

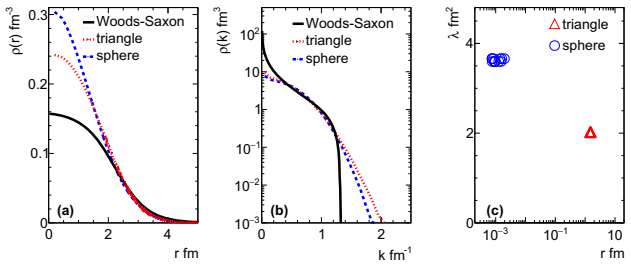

Fig. 3 (Color online) The (**a**) density, (**b**) momentum, and (**c**) width of wave packet distribution of different configurations of ^{12}C. Protons and neutrons are not distinguished in this study. The solid black lines shown in panels (a) and (b) represent the density and momentum distribution calculated by the Woods-Saxon distribution and under the free Fermi gas approximation

highest local density at the center of the nucleus is reached. This indicates that the nucleons are closer together in a spherical configuration than those in the other situations. In panel (b), the momentum distribution of three configurations is shown. Compared with the Woods-Saxon case, the momentum distribution initialized in the EQMD has a larger upper bound. In addition, this upper bound is highest in the triangle case related to the width distribution of the wave packets shown in panel (c). In the triangular case, the width of each particle is approximately 2 fm^2, whereas it is approximately 3.6 fm^2 in the spherical case. By contrast, although the spherical nucleus is compressed more tightly, the wave packet is also wider, and thus the r.m.s radii are similar for the two different configurations.

The time evolution of the hard photon production rate for ^{86}Kr + ^{12}C at E/A = 44 MeV, the average density, and the stopping power for this system are shown in Fig. 4a–c, respectively. We calculated the average density as follows:

$$\overline{\rho} = \frac{\int \rho^2 \mathrm{d}\mathbf{r}}{\int \rho \mathrm{d}\mathbf{r}} = \frac{\sum_{i,j}^{A} \int \rho_j(\mathbf{r})\rho_i(\mathbf{r})\mathrm{d}\mathbf{r}}{A}. \tag{15}$$

Here, A is the size of the reaction system, that is, the number of total nucleons in the system. It is clear that there is a strong positive correlation between the γ yield and the compression density, which is due to the frequent $p-n$ collisions. The minimum value of the γ yield rate and the average density of the system occur at near t = 90 fm/c, as indicated by the black dotted line. This means that the separation of the target- and project-like nuclei occurs. In other words, it constrains the time-selection range of the photons. We selected only those photons produced during the first compression stage of the system for analysis. At the same time, of note is the fact that the stopping power does not reach the maximum value during this process. In the literature, there are several forms of stopping power definitions. In this study, we adopt the energy-based isotropic ratio form [50], which is written as

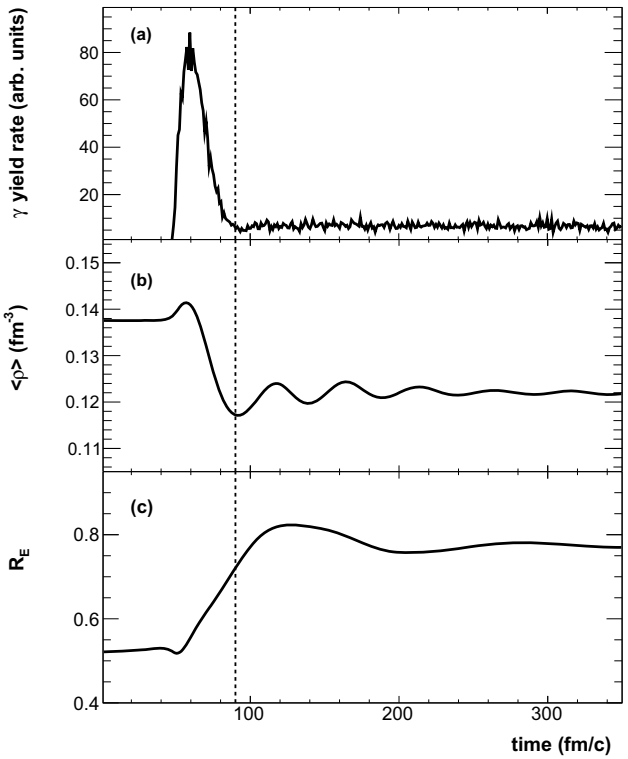

Fig. 4 **a** The time evolution of γ-production rate, **b** average density, and **c** stopping power for ^{86}Kr+^{12}C at E/A = 44 MeV. The black dotted line near time $t \approx 90$ fm/c represents the end of the first compression state

$$R_{\mathrm{E}} = \frac{\sum E_{\mathrm{T}}^{i}}{2\sum E_{\mathrm{l}}^{i}}. \tag{16}$$

Here, E_{T}^{i} represents the transverse kinetic energy, which is perpendicular to the beam direction, and E_{l}^{i} represents the longitudinal kinetic energy parallel to the beam direction. The stopping parameter is a physical quantity that not only describes the stopping power of nuclear matter, but also indicates the system thermalization. One can expect $R_{\mathrm{E}} = 1$ for a complete thermal equilibration and $R_{\mathrm{E}} < 1$ for a partial equilibration. In our case, it is clear that the system has not yet achieved a complete equilibrium during the pre-equilibrium stage.

Figure 5 shows the energy spectrum of hard photons emitted at angle $\theta_{\mathrm{lab}} = 40^{\circ}, 90^{\circ}, 150^{\circ}$ in the Lab frame for ^{86}Kr + ^{12}C at E/A = 44 MeV. The results calculated without considering dynamical wave packet effects, i.e., only including the center momentum of wave packets, is plotted in Fig. 5a, and the same quantities simulated by the modified EQMD model with triangular and spherical configurations are shown in Fig. 5b and c, respectively. It can cleanly be seen that the photon yield is seriously underestimated in the first situation. However, the energy spectra are reasonably reconstructed and experimental data

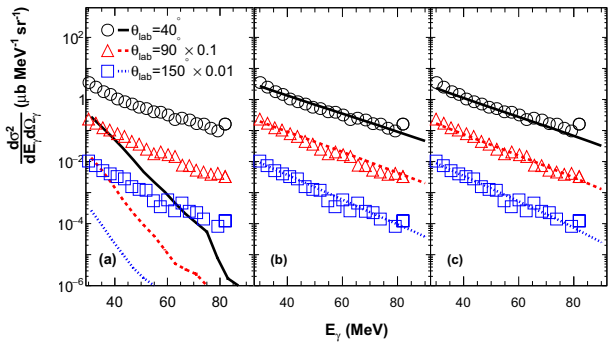

Fig. 5 (Color online) The energy spectrum of hard photons at angle $\theta_\gamma = 40°, 90°, 150°$ for ^{86}Kr + ^{12}C at E/A = 44 MeV. The results simulated by the EQMD without considering the dynamic wave packet effects are shown in (**a**). The case of a triangular configuration of 3α with our modified EQMD is shown in (**b**), and the spherical configuration is shown in (**c**). The lines represent the results of the theoretical calculation, and the open markers represent the experimental data obtained from [42]

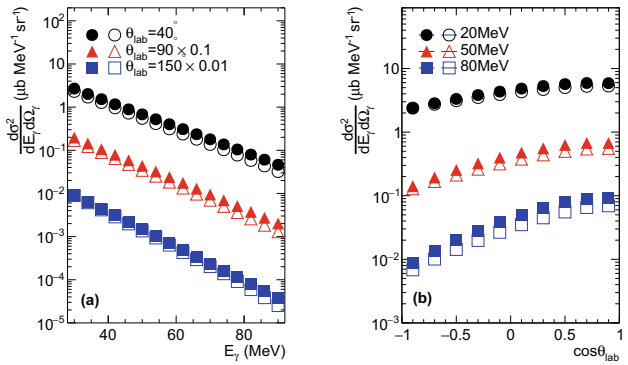

Fig. 6 (Color online) **a** The energy spectrum and **b** laboratory angular distributions of direct photons from the same reaction as Fig. 5 for different initial configurations of ^{12}C. The solid and open markers represent the triangular and spherical configurations, respectively

are reproduced regardless of the initial configurations adopted with our method described above. This confirms that the general method adopted by many QMD-type transport models that treat a nucleon as a point rather than a packet in a two-body scattering process will underestimate the available energy of an in-elastic process within the framework of the EQMD model, which was described in our previous study in more detail [43]. It should be noted that there is no contribution of wave packets to the kinetic energy for most QMD-type models. However, the contribution of a wave packet must be considered because the total kinetic energy is composed of three parts (Eq .3).

Figure 6a shows an energy spectrum comparison between a triangular and spherical configuration, and the

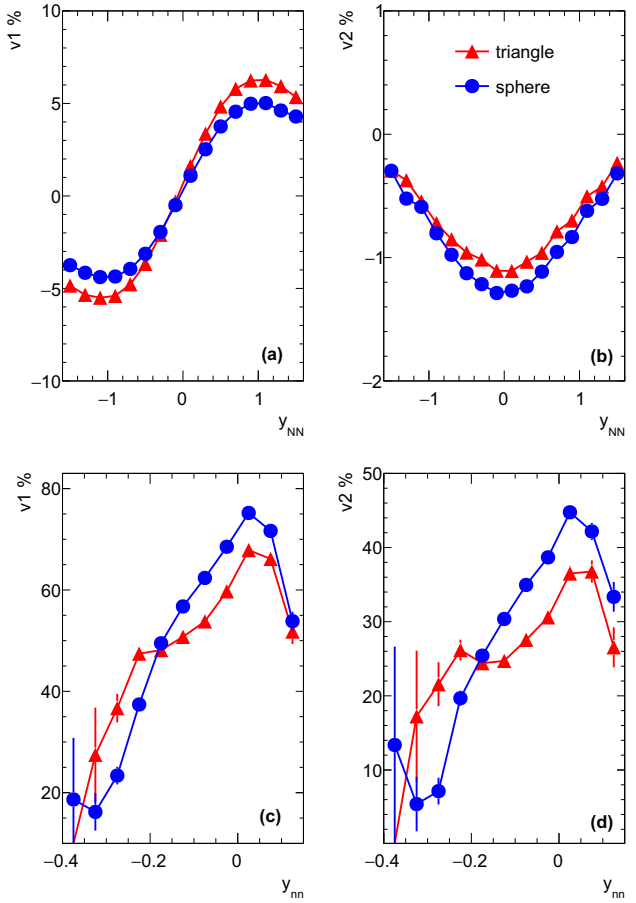

Fig. 7 (Color online) **a** Directed and **b** elliptic flows of direct photons versus rapidity for ^{86}Kr + ^{12}C at E/A = 44 MeV and an impact parameter of b = 5.0 fm, respectively. The same observations of free protons are shown in (**c**) and (**d**). The red triangles and blue spheres represent the triangular and spherical configurations of ^{12}C, respectively

laboratory angular distributions for the same reaction with photon energies of $E_\gamma = 20 \pm 3$ (cycle), 50 ± 3 (triangle), and 80 ± 3 (square) MeV are shown in Fig. 6b. The solid and open markers represent triangular and spherical configurations of ^{12}C. It seems that the energy spectrum of the triangular configuration is slightly higher and harder than that of the spherical configuration. A difference gradually appears with an increase in the γ energy. The same phenomenon is also visible within the angular spectrum of the Lab frame. This is closely related to Fig. 3b, where the upper bound of the kinetic energy in the triangular configuration is higher than that in the case of the spherical configuration. Therefore, the nucleon can have a higher available energy in the case of a triangular configuration.

Figure 7a and b show directed and elliptic flows of direct photons, respectively, and (c) and (d) show directed and elliptic flows for free protons. In the figures, red triangle and blue sphere markers represent the triangular and

spherical configurations of ^{12}C, respectively, and y_{NN} is the rapidity of direct photons in the nucleon-nucleon center of mass system and y_{nn} is the rapidity of emitted protons in the nucleus-nucleus center of mass system. According to previous research results [23], a large impact parameter of b = 5.0 fm is adopted. It is clear that v_1 of direct photons has a clear *S*-shape curve even in an asymmetrical system. However, the shape of the free protons' v_1 is irregular owing to the asymmetry between the projectile and target. This feature of direct photons can be explained by the geometrical equal-participant model [51] which describes a scenario in which there are the same number of particles from projectiles or targets taking part in the bremsstrahlung processing. Our results confirm this theory quite well, although different opinions regarding light systems [52] have been discussed. Another important reason is that direct photons are seldom absorbed by the surround nuclear matter, and thus the v_1 of direct photons can maintain its shape. In Fig. 7a, a positive flow parameter of direct photons, i.e., $F \equiv \mathrm{d}v_1/\mathrm{d}y_{NN}|_{y_{NN}=0} > 0$, can be observed. However, it is difficult to confirm the signal of the free proton in the anti-symmetry case shown in Fig. 7c owing to the serious effect by the surrounding matter. As is well known, nuclear attraction dominates within the Fermi-energy region where competition exists between the mean field and nucleon-nucleon collision. General speaking, for symmetrical systems, a negative flow parameter is expected if the attraction dominates. However, in the case of an asymmetrical system, this relationship seems unsatisfied again based on the EQMD simulation. In addition, a v_1 difference in direct photons between the triangular and spherical configurations can be observed in Fig. 7a. The amplitude of the directed flow calculated with the triangular configuration is slightly larger than that with the spherical configuration.

Figure 7b shows the elliptic flow of the direct photons. Photons tend to be emitted from the reaction plane. The difference in v_2 between the two ^{12}C configurations is observed. Compared with the triangle configuration case, the elliptic flow tends to emit out of the plane in the sphere configuration of the ^{12}C case. As opposed to direct photons, the free protons tend to be emitted in the plane, as shown in Fig. 7d. This v_2 anti-correlation between direct photons and free protons is in agreement with our previous results [38, 39, 53].

To judge the relationship between direct photons and free nucleons more carefully, we compare the directed flow of γ and the particles taking part in the bremsstrahlung process shown in Fig. 8. The original irregular curve was restored to a *S*-shape, and a negative flow parameter was observed. This strongly indicates an attractive dominant interaction between nucleons during the early stages. Moreover, v_1 of the triangular configuration is more intense, which is consistent with the above analysis. However, the curve is not fully symmetric; that is, it does not cross the origin, which indicates that the collective flow is influenced by the asymmetry of the system during the early stage. After a re-extraction, even in the case of an asymmetric system, the directed flow maintains an anti-correlation relationship between direct photons and free protons. It should be emphasized again that the collective motion of direct photons is only a reflection of the hadrons. However, this information will be intensely washed away by the surrounding nuclear matter throughout the reaction. Fortunately, the use of hard photons as an alternative choice can provide unique undistorted information regarding the reaction mechanism and geometric information of the nuclei at an early stage. It should also be noted that we did not set an energy range of the selected photons in the anisotropic flow calculation.

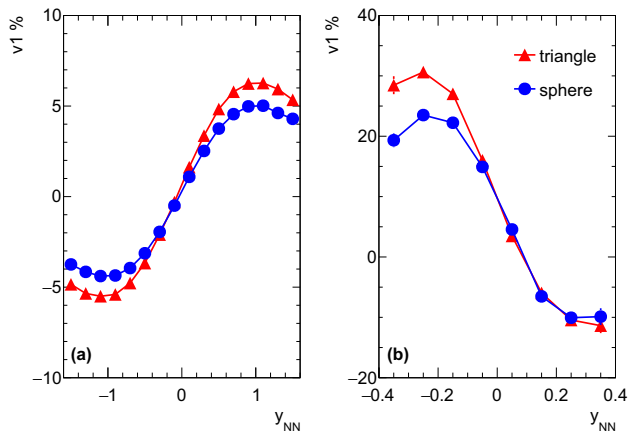

Fig. 8 (Color online) The directed flows of photons (**a**) and particles (**b**) taking part in the bremsstrahlung process. The marker is the same as that in Fig. 7

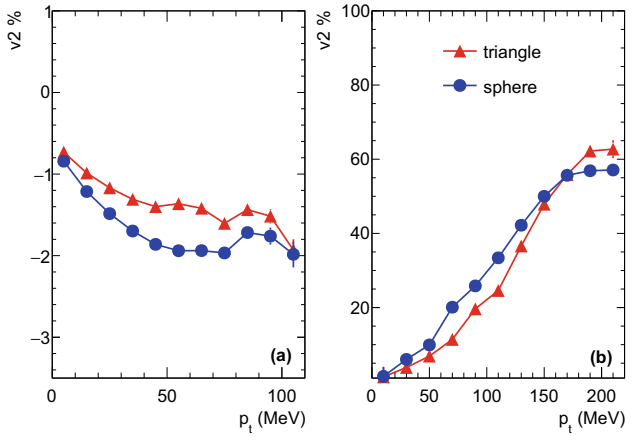

Fig. 9 (Color online) The rapidity dependence of elliptic flows for (**a**) direct photons and (**b**) free protons selected with a rapidity region $0.8y_t < y_{nn} < 0.8y_p$

The elliptic flows of direct photons and free protons as a function of rapidity are shown in Fig. 9a and b, respectively. The free protons were selected with a cut off of $0.8y_t < y_{nn} < 0.8y_p$. For the free protons, it was found that a strong transverse momentum dependence of the elliptic flow occurs, and its value increases extremely quickly with the transverse momentum at $p_t < 150$ MeV. However, for direct photons, the transverse momentum dependence is much weaker. As the transverse momentum increases, it quickly reaches saturation . In general, the free protons with a high transverse momentum escape at an earlier time, and those with a low transverse momentum experience more collisions. In other words, more frequent energy exchanges occur. Differing from the situation of free protons, all direct photons come from the early stage. Therefore, their transverse momenta are not determined by the emission time, which is why the elliptic flow of direct photons shows a small transverse momentum dependence. Based on this analysis result, we deduce that an obvious discrepancy in collective flows is already formed at the pre-equilibrium stage.

4 Conclusion

In summary, we first obtain a resonable energy and angular spectra of direct photons for ^{86}Kr + ^{12}C at E/A = 44 MeV within our modified EQMD model. The magnitude and slope of the hard photons were reasonably reproduced in comparison with the experimental data. This indicates that our modified EQMD model can deal with the bremsstrahlung process correctly within dynamical wave packets. Second, we investigated the collective flow of direct photons in peripheral collisions. A clear *S*-shaped curve of direct photons was obtained. By contrast, the directed flow of free protons loses a significant amount of information because of the intense absorption by the surrounding nuclear matter. In addition, differences in the collective flows of direct photons were observed between the triangular and spherical configurations of ^{12}C, which were initialized by the EQMD model in a self-consistent manner. We also analyzed the transverse momentum dependence of the elliptic flows. It was found that the direct photons have a more moderate dependence on the transverse momentum owing to the pre-equilibrium stage. In addition, it can be deduced that the discrepancy of the collective flow caused by the geometric effect appears during the extremely early stage. In total, it was found that a direct photon as an untwisted observable can reflect the early information of a system, even in an asymmetric system. In addition, the present study sheds light on an alternative probe to find a possible signal of the α-clustered structure in light nuclei by using direct photons.

Appendix

Strictly speaking, one should sample adequate times according to the Wigner function of a nucleon as follows:

$$\begin{aligned} w_i(\mathbf{r}) &= \rho_i(\mathbf{r}) \\ &= \left(\frac{1}{\pi\lambda_i}\right)^{\frac{3}{2}} \exp\left\{-\frac{1}{\lambda_i}\left(\mathbf{r}-\mathbf{R_i}\right)^2\right\}, \\ w_i(\mathbf{p}) &= \frac{w_i(\mathbf{r},\mathbf{p})}{\rho_i(\mathbf{r})} \\ &= \left(\frac{\lambda_i}{\pi\hbar^2}\right)^{\frac{3}{2}} \exp\left\{-\frac{\lambda_i}{\hbar^2}[\mathbf{p}-(\mathbf{P}_i+\delta_i\hbar\mathbf{R}_i-\delta_i\hbar\mathbf{r})]^2\right\}. \end{aligned} \tag{17}$$

Herein, $w_i(\mathbf{r})$ is the probability that the ith nucleon is at point $\mathbf{r}$, and $w_i(\mathbf{p})$ represents the probability of this nucleon with momentum $\mathbf{p}$ when its position is known at $\mathbf{r}$. It is easy to obtain certain quantities from Eq.17 as follows:

$$\begin{aligned} \overline{\mathbf{r}} &= \mathbf{R}_i, \\ \overline{\mathbf{r}^2} &= \mathbf{R}_i^2 + \frac{3}{2}\lambda_i, \\ \overline{\mathbf{p}} &= \mathbf{P}_i, \\ \overline{\mathbf{p}^2} &= \overline{[\mathbf{P}_i - \delta_i\hbar(\mathbf{r}-\mathbf{R}_i)]^2} + \frac{3\hbar^2}{2\lambda_i} \\ &= \mathbf{P}_i^2 + \overline{\delta_i^2\hbar^2(\mathbf{r}-\mathbf{R}_i)^2} + \frac{3\hbar^2}{2\lambda_i} \\ &= \mathbf{P}_i^2 + \frac{3\hbar^2}{2\lambda_i}\left(1+\lambda_i^2\delta_i^2\right). \end{aligned} \tag{18}$$

We also consider the zero-pointer kinetic energy into momentum sampling, our formulation is as follows:

$$\begin{aligned} \Delta\mathbf{p} &= \mathbf{p} - \mathbf{P}_i, \\ \mathbf{p}_i &= \mathbf{P}_i + \sqrt{1-\frac{1}{M_i}} \times \Delta\mathbf{p}. \end{aligned} \tag{19}$$

Here, $\mathbf{p}_i$ is the momentum of the nucleon after its zero-point kinetic energy is considered.

If one samples the coordinate and momentum adequately, the following can be easily proven:

$$\begin{aligned}\overline{\mathbf{p}_i^2} &= \overline{\left(\mathbf{P}_i + \sqrt{1-\frac{1}{M_i}} \times \Delta\mathbf{p}\right)^2} \\ &= \mathbf{P}_i^2 + \left(1-\frac{1}{M_i}\right) \times \frac{3\hbar^2}{2\lambda_i}\left(1+\lambda_i^2\delta_i^2\right), \\ \overline{T_i} &= \frac{\mathbf{P}_i^2}{2m_i} + \left(1-\frac{1}{M_i}\right) \times \frac{3\hbar^2}{4m_i\lambda_i}\left(1+\lambda_i^2\delta_i^2\right) \\ &= \frac{\mathbf{P}_i^2}{2m_i} + \frac{3\hbar^2\left(1+\lambda_i^2\delta_i^2\right)}{4m_i\lambda_i} - T_{\text{zero}}.\end{aligned} \tag{20}$$

Thus far, this proves that the kinetic energy obtained by this sampling method is consistent with the expected kinetic energy described by the Hamilton of the EQMD model. This part of the kinetic energy is dominant, namely in the "Fermi-motion" question in the study by Maruyama et al. [11]. In the actual calculation, it should be noted that there is an appropriate simplification for simulation purposes.

References

1. G. Gamow, Mass defect curve and nuclear constitution. Proc. R. Soc. Lond. Ser. A Contain. Pap. Math. Phys. Character **126**, 632–644 (1930). https://doi.org/10.1098/rspa.1930.0032
2. H.A. Bethe, R.F. Bacher, Nuclear physics a. stationary states of nuclei. Rev. Mod. Phys. **8**, 82–229 (1936). https://doi.org/10.1103/RevModPhys.8.82
3. H.A. Bethe, Nuclear physics b. nuclear dynamics, theoretical. Rev. Mod. Phys. **9**, 69–244 (1937). https://doi.org/10.1103/RevModPhys.9.69
4. L.R. Hafstad, E. Teller, The alpha-particle model of the nucleus. Phys. Rev. **54**, 681–692 (1938). https://doi.org/10.1103/PhysRev.54.681
5. F. Hoyle, On nuclear reactions occuring in very hot stars. I. The synthesis of elements from carbon to nickel. Astrophys. J. Suppl. Ser. **1**, 121 (1954). https://doi.org/10.1086/190005
6. S. Jin, L.F. Roberts, S.M. Austin et al., Enhanced triple-α reaction reduces proton-rich nucleosynthesis in supernovae. Nature **588**, 57 (2020). https://doi.org/10.1038/s41586-020-2948-7
7. H.L. Liu, D.D. Han, P. Ji et al., Reaction rate weighted multilayer nuclear reaction network. Chin. Phys. Lett. **37**, 112601 (2020). https://doi.org/10.1088/0256-307X/37/11/112601
8. H.L. Liu, D.D. Han, Y.G. Ma, et al., Network structure of thermonuclear reactions in nuclear landscape. Sci. China-Phys. Mech. Astron. **63**, 112062 (2020). https://doi.org/10.1007/s11433-020-1552-2
9. A. Ono, Antisymmetrized molecular dynamics for heavy ion collisions. Prog. Part. Nucl. Phys. **53**, 501–581 (2004). https://doi.org/10.1016/j.ppnp.2004.05.002
10. H. Feldmeier, J. Schnack, Molecular dynamics for fermions. Rev. Mod. Phys. **72**, 655–688 (2000). https://doi.org/10.1103/RevModPhys.72.655
11. T. Maruyama, K. Niita, A. Iwamoto, Extension of quantum molecular dynamics and its application to heavy-ion collisions. Phys. Rev. C **53**, 297–304 (1996). https://doi.org/10.1103/PhysRevC.53.297
12. W.B. He, Y.G. Ma, X.G. Cao et al., Giant dipole resonance as a fingerprint of α clustering configurations in ^{12}C and ^{16}O. Phys. Rev. Lett. **113**, 032506 (2014). https://doi.org/10.1103/PhysRevLett.113.032506
13. W.B. He, Y.G. Ma, X.G. Cao et al., Dipole oscillation modes in light alpha-clustering nuclei. Phys. Rev. C **94**, 014301 (2016). https://doi.org/10.1103/PhysRevC.94.014301
14. B.S. Huang, Y.G. Ma, W.B. He, Photonuclear reaction as a probe for α-clustering nuclei in the quasi-deuteron region. Phys. Rev. C **95**, 034606 (2017). https://doi.org/10.1103/PhysRevC.95.034606
15. J. He, S. Zhang, Y.G. Ma et al., Clustering structure effect on Hanbury-BrowncTwiss correlation in ^{12}C +^{197} Au 12C+197Au collisions at 200 GeV. Eur. Phys. J. A **56**, 52 (2020). https://doi.org/10.1140/epja/s10050-019-00002-0
16. B.S. Huang, Y.G. Ma, Two-proton momentum correlation from photodisintegration of α-clustering light nuclei in the quasideuteron region. Phys. Rev. C **101**, 034615 (2020). https://doi.org/10.1103/PhysRevC.101.034615
17. B.S. Huang, Y.G. Ma, Emission time sequence of neutrons and protons as probes of α-clustering structure. Chin. Phys. C **44**, 094105 (2020). https://doi.org/10.1088/1674-1137/44/9/094105
18. W. Broniowski, E.R. Arriola, Signatures of alpha clustering in light nuclei from relativistic nuclear collisions. Phys. Rev. Lett. **112**, 112–501 (2020). https://doi.org/10.1103/PhysRevLett.112.112501
19. S. Zhang, Y.G. Ma, J.H. Chen et al., Nuclear cluster structure effect on elliptic and triangular flows in heavy-ion collisions. Phys. Rev. C **95**, 064904 (2017). https://doi.org/10.1103/PhysRevC.95.064904
20. S. Zhang, Y.G. Ma, J.H. Chen et al., Collective flows of α-clustering 12c + 197au by using different flow analysis methods. Eur. Phy. J. A **54**, 161 (2018). https://doi.org/10.1140/epja/i2018-12597-y
21. S.H. Lim, J. Carlson, C. Loizides et al., Exploring new small system geometries in heavy ion collisions. Phys. Rev. C **99**, 04490 (2019). https://doi.org/10.1103/PhysRevC.99.044904
22. C.C. Guo, Y.G. Ma, Z.D. An et al., Influence of α-clustering configurations in ^{16}O + ^{197}Au collisions at fermi energy. Phys. Rev. C **99**, 044607 (2019). https://doi.org/10.1103/PhysRevC.99.044607
23. C.C. Guo, W.B. He, Y.G. Ma, Collective flows of ^{16}o+^{16}o collisions with α-clustering configurations. Chin. Phys. Lett. **34**, 092101 (2017). https://doi.org/10.1088/0256-307x/34/9/092101
24. Y.A. Li, S. Zhang, Y.G. Ma, Signatures of α-clustering in ^{16}O by using a multiphase transport model. Phys. Rev. C **102**, 054907 (2020). https://doi.org/10.1103/PhysRevC.102.054907
25. W. Reisdorf, H.G. Ritter, Collective flow in heavy-ion collisions. Ann. Rev. Nuclear Particle Sci. **47**, 663–709 (1997). arXiv: https://doi.org/10.1146/annurev.nucl.47.1.663, https://doi.org/10.1146/annurev.nucl.47.1.663
26. N. Herrmann, J.P. Wessels, T. Wienold, Collective flow in heavy-ion collisions. Ann. Rev. Nuclear Particle Sci. **49**, 581–632 (1999). arXiv:https://doi.org/10.1146/annurev.nucl.49.1.581, https://doi.org/10.1146/annurev.nucl.49.1.581
27. A.E. Glassgold, W. Heckrotte, K.M. Watson, Collective excitations of nuclear matter. Ann. Phys. **6**, 1–36 (1959). https://doi.org/10.1016/0003-4916(59)90037-5
28. W. Scheid, H. Müller, W. Greiner, Nuclear shock waves in heavy-ion collisions. Phys. Rev. Lett. **32**, 741–745 (1974). https://doi.org/10.1103/PhysRevLett.32.741
29. H.A. Gustafsson, H.H. Gutbrod, B. Kolb et al., Collective flow observed in relativistic nuclear collisions. Phys. Rev. Lett. **52**, 1590–1593 (1984). https://doi.org/10.1103/PhysRevLett.52.1590
30. R.E. Renfordt, D. Schall, R. Bock, et al., Stopping power and collective flow of nuclear matter in the reaction ar+pb at 0.8 gev/

u. Phys. Rev. Lett. **53**, 763–766 (1984). https://doi.org/10.1103/PhysRevLett.53.763
31. C.A. Ogilvie, W. Bauer, D.A. Cebra et al., Disappearance of flow and its relevance to nuclear matter physics. Phys. Rev. C **42**, R10–R14 (1990). https://doi.org/10.1103/PhysRevC.42.R10
32. C.L. Zhou, Y.G. Ma, D.Q. Fang et al., Correlation between elliptic flow and shear viscosity in intermediate-energy heavy-ion collisions. Phys. Rev. C **90**, 057601 (2014). https://doi.org/10.1103/PhysRevC.90.057601
33. G.D. Westfall, W. Bauer, D. Craig et al., Mass dependence of the disappearance of flow in nuclear collisions. Phys. Rev. Lett. **71**, 1986–1989 (1993). https://doi.org/10.1103/PhysRevLett.71.1986
34. B.A. Li, A.T. Sustich, Differential flow in heavy-ion collisions at balance energies. Phys. Rev. Lett. **82**, 5004–5007 (1999). https://doi.org/10.1103/PhysRevLett.82.5004
35. U. Heinz, R. Snellings, Collective flow and viscosity in relativistic heavy-ion collisions. Annu. Rev. Nucl. Part. Sci. **63**, 123 (2013). https://doi.org/10.1146/annurev-nucl-102212-170540
36. C. Shen, L. Yan, Recent development of hydrodynamic modeling in heavy-ion collisions. Nucl. Sci. Tech. **31**, 122 (2020). https://doi.org/10.1007/s41365-020-00829-z
37. M. Waqas, F.H. Liu, L.L. Li et al., Effective (kinetic freeze-out) temperature, transverse flow velocity, and kinetic freeze-out volume in high energy collisions. Nucl. Sci. Tech. **31**, 109 (2020). https://doi.org/10.1007/s41365-020-00821-7
38. G.H. Liu, T.Z. Yan, Y.G. Ma et al., Anisotropic flows of nuclear clusters and hard photons in intermediate energy heavy ion collisions. Int. J. Mod. Phys. E **17**, 1850–1864 (2008). https://doi.org/10.1142/S0218301308010830
39. G. Liu, Y.G. Ma, X. Cai et al., Azimuthal asymmetry of direct photons in intermediate energy heavy-ion collisions. Phys. Lett. B **663**, 312–316 (2008). https://doi.org/10.1016/j.physletb.2008.04.037
40. Y.G. Ma, G.H. Liu, X.Z. Cai et al., Hard-photon flow and photon-photon correlation in intermediate-energy heavy-ion collisions. Phys. Rev. C **85**, 024618 (2012). https://doi.org/10.1103/PhysRevC.85.024618
41. S.S. Wang, Y.G. Ma, X.G. Cao et al., Hard-photon production and its correlation with intermediate-mass fragments in a framework of a quantum molecular dynamics model. Phys. Rev. C **102**, 024620 (2020). https://doi.org/10.1103/PhysRevC.102.024620
42. R. Bertholet, M.K. Njock, M. Maurel et al., High energy gamma-ray production from 44 mev/a 86kr bombardment on nuclei. Nucl. Phys. A **474**, 541–556 (1987). https://doi.org/10.1016/0375-9474(87)90630-0
43. C.Z. Shi, Y.G. Ma, X.G. Cao et al., Direct photon emission and influence of dynamical wave packets in an extended quantum molecular dynamics model. Phys. Rev. C **102**, 014601 (2020). https://doi.org/10.1103/PhysRevC.102.014601
44. A. Ono, H. Horiuchi, T. Maruyama et al., Antisymmetrized version of molecular dynamics with two nucleon collisions and its application to heavy ion reactions. Prog. Theor. Phys. **87**, 1185–1206 (1992). https://doi.org/10.1143/PTP.87.1185
45. W. Bauer, G.F. Bertsch, W. Cassing et al., Energetic photons from intermediate energy proton- and heavy-ion-induced reactions. Phys. Rev. C **34**, 2127–2133 (1986). https://doi.org/10.1103/PhysRevC.34.2127
46. A.M. Poskanzer, S.A. Voloshin, Methods for analyzing anisotropic flow in relativistic nuclear collisions. Phys. Rev. C **58**, 1671–1678 (1998). https://doi.org/10.1103/PhysRevC.58.1671
47. Y.G. Ma, W.Q. Shen, J. Feng et al., Rotational behavior in intermediate-energy heavy-ion collisions. Phys. Rev. C **48**, R1492–R1496 (1993). https://doi.org/10.1103/PhysRevC.48.R1492
48. Y.G. Ma, W.Q. Shen, Correlation-functions and the disappearance of rotational collective motion in nucleus-nucleus collisions below 100 mev/nucleon. Phys. Rev. C **51**, 3256–3263 (1995). https://doi.org/10.1103/PhysRevC.48.R1492
49. T. Furuta, K.H.O. Hasnaoui, F. Gulminelli, et al., Monopole oscillations in light nuclei with a molecular dynamics approach. Phys. Rev. C **82**. https://doi.org/10.1103/PhysRevC.82.034307
50. G.Q. Zhang, Y.G. Ma, X.G. Cao, et al., Unified description of nuclear stopping in central heavy-ion collisions from 10 A MeV to 1.2 A GeV. Phys. Rev. C **84**, 034612 (2011). https://doi.org/10.1103/PhysRevC.84.034612
51. H. Nifenecker, J. Bondorf, Nuclear electromagnetic bremsstrahlung: a new tool for studying heavy-ion reactions. Nucl. Phys. A **442**, 478–508 (1985). https://doi.org/10.1016/S0375-9474(85)80028-2
52. N. Gan, K.T. Brinkmann, A.L. Caraley et al., Neutron-proton bremsstrahlung from low-energy heavy-ion reactions. Phys. Rev. C **49**, 298–303 (1994). https://doi.org/10.1103/PhysRevC.49.298
53. S.S. Wang, Y.G. Ma, X.G. Cao et al., Azimuthal anisotropy and multiplicities of hard photons and free nucleons in intermediate-energy heavy-ion collisions. Eur. Phys. J. A **56**, 254 (1993). https://doi.org/10.1140/epja/s10050-020-00264-z